Hydrodynamics of a confined active Belousov-Zhabotinsky droplet

K. V. S. Chaithanya, Shreyas A. Shenoy, and Pratyush Dayal*
Polymer Engineering Research Laboratory, Department of Chemical Engineering, Indian Institute of Technology Gandhinagar, Gujarat 382055, India

(Received 6 July 2022; accepted 2 December 2022; published 23 December 2022)

Self-sustained locomotion of synthetic droplet swimmers has been of great interest due to their ability to mimic the behavior of biological swimmers. Here we harness the Belousov-Zhabotinsky (BZ) reaction to induce Marangoni stresses on the fluid-droplet interface and elucidate the spontaneous locomotion of active BZ droplets in a confined two-dimensional channel. Our approach employs the lattice Boltzmann method to simulate a coupled system of multiphase hydrodynamics and BZ-reaction kinetics. Our investigation reveals the mechanism underlying the propulsion of active BZ droplets, in terms of convective and diffusive fluxes and deformation of the droplets. Furthermore, we demonstrate that by manipulating the degree of confinement, strength, and nature of coupling between surface tension and active species' concentration, the motion of the BZ droplet can be directed. In addition, we are able to capture two different kinds of droplet behaviors, namely, sustained and stationary, and establish conditions for the sustained long-time motion. We envisage that our findings can be used not only to understand the mechanics of biological swimmers but also to design reaction-driven self-propelled systems for a variety of biomimetic applications.

DOI: 10.1103/PhysRevE.106.065103

I. INTRODUCTION

In the past few decades, there has been great interest in developing model systems that can mimic the mechanics of biological entities. An active droplet is one such system that has been extensively used to understand locomotion and swarming behavior of biological systems. Although several mechanisms have been harnessed to induce self-propulsion in fluid droplets [1–3], they can be broadly classified into two major categories: physical and interfacial. In physical mechanisms, self-propelling constituents such as Janus colloids, magnetotactic bacteria, and cytoskeletal filaments are encapsulated within a fluid droplet [4–8]; the motion of these constituents eventually drives the droplet. On the other hand, the interfacial mechanisms rely on the Marangoni stresses intrinsically induced by the surface tension gradient along the droplet interface [9–13] facilitated by surface-active species (surfactants). Here we focus on understanding the dynamics of a channel-confined active droplet driven by a Belousov-Zhabotinsky (BZ) reaction using the lattice Boltzmann method (LBM). Using numerical simulations, we identify and characterize the different possible behaviors of a BZ droplet in a confined environment. Our findings reveal the combined effect of confinement and reaction-induced Marangoni stresses on active droplet dynamics and can be utilized to understand the propulsion of biological entities such as cells and natural and synthetic swimmers.

Based on the mechanism for generating surface tension gradients, which eventually drive the particles or droplets by generating fluids flows at large length scales, the active self-propelled systems can be broadly classified into two different categories: solubilization based and chemical reaction based [1,2]. Needless to say, these self-propelled systems are primarily two-phase systems wherein the active object is the dispersed phase and the surrounding fluid is the continuous phase. In the solubilization-based mechanism, the dissolution of a solute from an active object (solid or liquid) into the surrounding medium gives rise to surface tension gradients at the interface that propels the active entity away from the low-surface-tension region [11,14]. As the active object starts to swim, it disturbs the surrounding fluid and thereby generates Marangoni flows that in turn influence the distribution of the solute. In the reaction-based mechanism, on the other hand, it is the chemical reaction between various entities, along with the diffusion of the surfactant, that induces the surface tension gradient; the reaction, however, can be either heterogeneous or homogeneous [9,11,13,15,16].

The motion of the active object generated via dissolution and the heterogeneous-reaction-based mechanism bears direct dependence on its mass and thus as time progresses the mass reduces either by dissolution or a reaction and the object tends to speed up [11,14,17,18]. On the other hand, active systems based on a homogeneous chemical reaction such as the self-oscillating BZ reaction have several advantages over other mechanisms from various perspectives. First, the constituents of the BZ reaction generate asymmetric spatiotemporal patterns inherently without any external intervention. Moreover, the spatiotemporal oscillations and corresponding flows are sustained for longer periods of time compared to other systems. Second, the kinetics of the BZ reaction can be tuned by an external stimulus and thus provides a controlling mechanism for the object's motion. For instance, it is known that the speed and the direction of chemical waves

*pdayal@iitgn.ac.in

in photosensitive BZ reactions [16,19] and BZ hydrogels can be controlled by nonuniform illumination [20]. Third, unlike the solubilization-based mechanisms, where the mass of the active object decreases as it moves, chemical-reaction-based systems have no such limitations due to the continuous consumption and generation of the reactive species. Finally, understanding the hydrodynamic flows induced by the BZ-reaction-based active systems provides insight into signaling waves and large-scale cellular flows observed in biological systems. For instance, the patterns in the concentration of a morphogen [21,22] closely resemble the spatiotemporal patterns observed in self-oscillating systems such as the BZ reaction.

Several researchers have harnessed the chemical oscillations in the BZ reaction to generate Marangoni stresses that produce hydrodynamic flows and induce droplet motion. One of the first demonstrations of these flows in a BZ-reaction system is based on the experiments with a flat fluid-fluid interface and a millimeter-size droplet [23] wherein the BZ droplet exhibits time-periodic oscillations with a frequency that is synchronous with the chemical wave propagating inside the droplet. Later, by employing a photosensitive BZ reaction, a strategy to control the direction of propulsion of these active droplets by spatially varying illumination [16] was demonstrated. In both these systems, the propulsion of the BZ droplet is dependent upon the redox state of the BZ catalyst. In an alternative strategy, the interfacial reaction between one of the BZ species with the surfactant has been utilized to drive the motion of active BZ droplets [1,2,9,13,24–26]. In these cases, one of the intermediates diffuses from the bulk of the droplet to the surfactant-laden interface and reacts with the surfactant to form a complex. This complex has a different surface tension, which generates the surface tension gradient along the droplet-fluid interface that drives the propulsion. A detailed reaction mechanism of active BZ droplets driven by the interfacial reaction between bromine and the surfactant was recently established [9,13]; it was shown that, by virtue of the interfacial reaction, the BZ droplet exhibits a ballistic motion in a reduced state and random motion in an oxidized state [9,13].

Recently, it was demonstrated that the propulsion dynamics of BZ droplets is greatly enhanced by using the nanocatalyzed BZ reaction. In particular, it was experimentally demonstrated that the velocity of a BZ droplet is greatly enhanced by using bare ceria nanosheets [27] and nanoparticle-decorated graphene nanosheets [13]. The increase in propulsion speed of the nanocatalyzed BZ droplets has been attributed to the combined effect of enhanced reaction kinetics and the corresponding Marangoni flow. Many of the previously described experiments therefore have developed strategies to employ the BZ formulation for driving the droplet motion in unbounded environments; the typical scenarios, however, are often confined and complex. Moreover, it is necessary to understand the effect of confinement on reaction-driven droplets to employ them for any task in microfluidic devices [28]. Henceforth, in this study we investigate the effect of confinement on the motion of an active droplet driven by the self-oscillating BZ reaction.

In parallel with the previously described experiments, several theoretical [29–34] and numerical [35–37] works have also investigated the dynamics of active droplets. In analytical studies, the flow fields and swimming velocities were calculated for a defined surface tension profile along the interface [29]. On the other hand, numerical simulations were employed to solve the coupled problems involving chemical reactions and multiphase hydrodynamics. One of the first numerical models for capturing the motion of an active droplet driven by the BZ reaction was based on the LBM [37]. Here the researchers modeled the BZ kinetics using the Oregonator model and analyzed the propulsion dynamics of an active BZ droplet with decaying concentration of the reactive species, i.e., the sustained chemical oscillations of the BZ reaction was not taken into consideration. These investigations demonstrated a strong correlation between a chemical wave propagating inside the droplet and the swimming speed of the BZ droplet; however, the effect of confinement was neglected. In an alternative approach, the diffusion-advection-reaction equations were formulated using the phase-field mechanism and the dynamics of active droplets were investigated by coupling it with hydrodynamic equations [36]. Although in these investigations different swimming states, namely, stable swimming, stationary and oscillating, were identified based on the Marangoni number, the effect of confinement on the swimming dynamics was neglected. In contrast, the LBM was developed to investigate the effect of confinement on the dynamics of active droplets without incorporating the chemical reaction kinetics [33]. In particular, the hydrodynamic equations are coupled with convection-diffusion equations for surfactants and phase-field parameters to chart the active droplet motion in a confined channel.

To summarize, many previous studies neglected the combined effect of reaction kinetics and confinement on the dynamics of a BZ active droplet. A thorough investigation of the interplay between reaction kinetics and confinement on the dynamics of an active BZ droplet is therefore necessary to employ them for any application in microfluidic devices and to get insight into the biological scenarios, for example, the mechanism of cell motion in response to chemical signals. In this work, therefore, we investigate the propulsion dynamics of an active droplet driven by a BZ reaction in a channel using the LBM. The schematic of the configuration considered in this work is shown in Fig. 1. We consider an active BZ droplet of diameter D, initially located at the center of the channel of height $H = \alpha D$, where α denotes the size ratio. Furthermore, consistent with experimental studies [9–13], we restrict our analysis to two dimensions as BZ droplets are typically denser than the surrounding fluid and consequently exhibit planar motion on the surface of the substrate. Moreover, unlike previous studies [37], we consider the reaction parameters that correspond to sustained chemical oscillations in the BZ reaction. We assert that the framework presented here can be easily extended to investigate the dynamics of BZ droplets in three dimensions. In the experiments, however, the effect of the third dimension can be probed by considering a neutrally buoyant BZ droplet.

The rest of the article is organized as follows. In Sec. II we start by discussing the kinetics of the BZ reaction, which is followed by the governing equations for fluid flow and the phase-field approach for interface tracking. Subsequently, we present the lattice Boltzmann algorithm that is used to solve

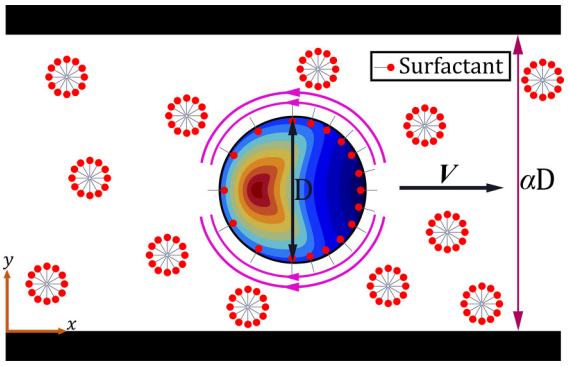

FIG. 1. Schematic representation of the BZ droplet in a surrounding fluid confined in a two- dimensional channel. The diameter of the BZ droplet is D and channel height is αD. The blue and red colors inside the droplet represent the low and high concentration of active species, respectively. The curved arrows along the droplet represent Marangoni flow and the swimming velocity of the droplet is indicated by $\boldsymbol{V}$.

the coupled nonlinear equations involving chemical kinetics and multiphase hydrodynamics. We end Sec. II by listing the parameters that are used in our simulations. In Sec. III we validate our LBM framework and present the results by characterizing the dynamics of a channel-confined active droplet for varying degree of coupling between concentration, surface tension, and confinement. We briefly summarize in Sec. IV.

II. METHODOLOGY

A. Active droplet and BZ reaction

As described in the foregoing paragraphs, the droplet phase in our system undergoes a BZ reaction that results in the chemical oscillations of the key species confined within the droplet. Specifically, we consider two reactive species 1 and 2 whose concentrations c_1 and c_2 show rhythmic variations consistent with chemical oscillations observed in the BZ reaction. These sustained oscillations together with the advection-diffusion of the chemical species generate traveling chemical waves that manifest as target or spiral patterns in the droplet. Thus, the spatiotemporal evolution of the concentration of the two species, i.e., c_1 and c_2, is governed by the coupled advection-diffusion equations, represented in terms of c_k as

$$\frac{\partial c_k}{\partial t} + \boldsymbol{u}\cdot\nabla c_k = \nabla\cdot(D_k\nabla\mu_k) + J_k, \quad k = 1, 2, \tag{1}$$

where $\boldsymbol{u}$ is the local fluid velocity and D_k, μ_k, and J_k are the diffusion coefficient, chemical potential, and source term for species k, respectively. The left-hand side of the equation describes the advection of the species k due to the motion of the fluid, whereas the first term on the right-hand side describes the diffusion and the second term incorporates the generation and depletion of species k by a chemical reaction. For the specific case of the BZ reaction, the source terms are represented by the two-variable Oregonator model [38] given by

$$J_1 = \frac{1}{\epsilon}\left(c_1(1-c_1) - \frac{bc_2(c_1-a)}{c_1+a}\right), \tag{2}$$

$$J_2 = c_1 - c_2, \tag{3}$$

where the dimensionless parameters a, b, and ϵ represent a reaction rate constant, stoichiometric factor, and reagent concentration, respectively. In the context of the BZ reaction, the species c_1 and c_2 are often referred to as the activator and oxidized catalyst, respectively. It is known that the chemical oscillations in the BZ reaction are driven by the periodic reduction and oxidation of the catalyst and consequently c_2 periodically switches between the low ($c_2 = c_2^{\min}$) and high ($c_2 = c_2^{\max}$) values. The redox cycles in c_2 induce periodic oscillations in c_1 between the low ($c_1 = c_1^{\min}$) and high ($c_1 = c_1^{\max}$) values. From a mathematical standpoint, the oscillations in the BZ reactions occur when the fixed point represented by $J_1 = J_2 = 0$, i.e.,

$$c_1^{\rm eq} = c_2^{\rm eq} = \frac{1}{2}\left[1 - b - a + \sqrt{b^2 + (1+a)^2 + b(6a-2)}\right], \tag{4}$$

loses stability via the Hopf bifurcation, as the parameters in Eq. (4) are varied [39]. In other words, the Hopf bifurcation curve demarcates the regions of sustained and decayed oscillations that are computed from the Jacobian matrix [40]

$$M_J = \begin{bmatrix} \frac{\partial J_1}{\partial c_1} & \frac{\partial J_1}{\partial c_2} \\ \frac{\partial J_2}{\partial c_1} & \frac{\partial J_2}{\partial c_2} \end{bmatrix} = \begin{bmatrix} \frac{1}{\epsilon}\left(1 - 2\,c_1 + \frac{b(c_1-a)}{(c_1+a)^2}c_2 - \frac{bc_2}{ac_1}\right) & \frac{1}{\epsilon}\frac{b(a-c_1)}{a+c_1} \\ 1 & -1 \end{bmatrix} \tag{5}$$

using the condition $\mathrm{Tr}(M_J) = 0$ that results in the relation

$$\epsilon = 1 - 2c_1^{\rm eq} - 2ba\frac{c_1^{\rm eq}}{\left(a + c_1^{\rm eq}\right)^2}. \tag{6}$$

For a given a, the locus of the points governed by Eq. (6) demarcates the two regions in the b–ϵ phase space and is known as a bifurcation curve. Note that the eigenvalues of M_J, given by $2\lambda_{1,2} = -\mathrm{Tr}(M_J) \pm \sqrt{\mathrm{Tr}(M_J)^2 - 4\,\mathrm{Det}(M_J)}$, become purely complex at the Hopf bifurcation. Thus, in the BZ reaction the sustained chemical oscillations are observed when $\mathrm{Tr}(M_J) > 0$ and decayed oscillations are observed otherwise.

Here we assume that the species 1 acts as a surfactant [37] and its concentration is altered at the droplet interface due to the BZ reaction [41]. This asymmetric distribution of c_1 on the droplet interface creates a surface tension gradient and drives the droplet motion by virtue of Marangoni stresses. In order to capture the hydrodynamics of the droplet motion, the interface between the droplet and the surrounding fluid needs to be tracked at all times; we present this framework in the following sections.

B. Hydrodynamics and phase-field modeling

The hydrodynamics of our system is governed by the continuity and momentum equations

$$\nabla\cdot\boldsymbol{u} = 0, \tag{7}$$

$$\rho\left(\frac{\partial\boldsymbol{u}}{\partial t} + \boldsymbol{u}\cdot\nabla\boldsymbol{u}\right) = -\nabla p + \nabla\cdot\boldsymbol{\Pi} + \boldsymbol{F}_s, \tag{8}$$

where ρ is the fluid density, p is the hydrodynamic pressure, $\boldsymbol{\Pi} = \eta[\nabla\mathbf{u} + (\nabla\mathbf{u})^{\rm T}]$ is the viscous stress tensor with

dynamic viscosity η, and $\boldsymbol{F}_s$ is the force arising due to surface tension. Here we have assumed that both the droplet and surrounding fluid are incompressible and Newtonian. Although, the fluid flow in the entire multiphase domain (droplet and surrounding fluid) is governed by the above equations, we introduce a phase-field variable ϕ to distinguish between the phases. This phase-field variable takes the value 1 for the droplet and 0 for the surrounding fluid and evolves as [42]

$$\frac{\partial \phi}{\partial t} + \boldsymbol{u} \cdot \nabla \phi = \nabla \cdot \left[M \left(\nabla \phi - \frac{4}{\zeta} \phi (1-\phi) \hat{\boldsymbol{n}} \right) \right], \quad (9)$$

where M and ζ are the respective interface mobility and thickness and $\hat{\boldsymbol{n}}$ is the unit normal vector pointing away from the droplet interface, defined as

$$\hat{\boldsymbol{n}} = \frac{\nabla \phi}{|\nabla \phi|}. \quad (10)$$

The left-hand side of Eq. (9) describes the advection of ϕ due to fluid velocity $\boldsymbol{u}$, whereas the right-hand side captures the effect of surface tension and curvature on the interface dynamics [42]. The variation of ϕ across the interface, located at $\boldsymbol{r} = \boldsymbol{r}_0$, is given by [43]

$$\phi(\boldsymbol{r}) = \frac{1}{2} \left[1 - \tanh \left(\frac{2}{\zeta} |\boldsymbol{r} - \boldsymbol{r}_0| \right) \right]. \quad (11)$$

Using the free-energy approach [44], the chemical potential of binary fluids is calculated as

$$\mu_\phi = 4\beta\phi\left(\phi - \tfrac{1}{2}\right)(\phi - 1) - \kappa \nabla^2 \phi, \quad (12)$$

where β and κ are related to the surface tension σ as $\beta = 12\sigma/\zeta$ and $\kappa = 3\sigma\zeta/2$, respectively. The first term corresponds to the bulk free energy that has minima at $\phi = 0, 1$, while the second term represents the contribution from the interfacial tension. The expression for $\boldsymbol{F}_s$ in terms of ϕ is then written as

$$\boldsymbol{F}_s = \mu_\phi \nabla \phi. \quad (13)$$

It is worth mentioning here that the interfacial coefficient κ accounts for the energy penalty associated with the fluid-fluid interface. Thus, to incorporate the effect of the surfactant (species 1) in our system we write

$$\kappa = \kappa_0 \left\{ 1 + \Delta\kappa \tanh \left[\chi \left(c_1 - c_1^{\text{ref}} \right) \right] \right\}, \quad (14)$$

where $\kappa = \kappa_0$ when c_1 is in the reference state c_1^{ref} and the constants $\Delta\kappa$ and χ are the coupling parameters [37]. When $c_1 > c_1^{\text{ref}}$, the surface tension between the two fluids is reduced when $\Delta\kappa < 0$ and increases otherwise; thus, the value of c_1^{ref} is chosen to represent the minimum concentration $c_1^{\min}$ in our system. Finally, the preferential adsorption or desorption of surfactant at the interface of the two fluids also affects the chemical potential μ_1 and hence the diffusion of species 1 [see Eq. (1)]. Thus, the expression for μ_1 is modified in terms of ϕ as [37]

$$\mu_1 = \gamma_1 c_1 + \frac{d\kappa}{dc_1} \frac{|\nabla \phi|^2}{2}. \quad (15)$$

On the other hand, as species 2 is not surface active, the chemical potential μ_2 remains unaffected and thus we take $\mu_2 = \gamma_2 c_2$, where γ_1 and γ_2 are constants known as activity coefficients.

C. Lattice Boltzmann method

The governing equations of our system, represented by Eqs. (1) and (7)–(9), are solved using the multicomponent two-fluid LBM. Our implementation begins by defining the four probability distribution functions $f_j^{(k)}$, i.e., one for each advection-diffusion of species 1 ($k = 1$) and 2 ($k = 2$), one for phase-field variable ($k = 3$), and one for momentum ($k = 4$). In general, all $f_j^{(k)}$ evolve according to the Bhatnagar-Gross-Krook approximated discretized LB equation as

$$f_j^{(k)}(\boldsymbol{r} + \boldsymbol{e}_j \Delta t,\ t + \Delta t) = f_j^{(k)}(\boldsymbol{r}, t) - \frac{f_j^{(k)} - f_j^{(k),\,\text{eq}}}{\tau_k} + \Delta t S_j^{(k)}, \quad (16)$$

where the subscript j signifies the lattice direction, $f_j^{(k),\,\text{eq}}$ is the equilibrium distribution function, $S_j^{(k)}$ is the source term, $\boldsymbol{e}_j$ is the lattice velocity defined according to the D_2Q_9 scheme as

$$\boldsymbol{e}_j = \begin{cases} c(0,0), & j = 0 \\ c(\cos\theta_j, \sin\theta_j), & \theta_j = (j-1)\pi/2,\ \ j = 1\text{–}4 \\ c(\cos\theta_j, \sin\theta_j), & \theta_j = (2j-9)\pi/4,\ \ j = 5\text{–}8, \end{cases} \quad (17)$$

and τ_k is the relaxation time that defines the diffusive property $N_k = c_s^2(\tau_k - \frac{1}{2})\Delta t$. Here N_k is the diffusivity of species 1 ($k = 1$) and 2 ($k = 2$), interface mobility M for the phase-field variable ($k = 3$), and kinematic viscosity ν of the fluids ($k = 4$). In addition, $c_s^2 = \frac{c}{\sqrt{3}}$ is the speed of sound with $c = \frac{\Delta x}{\Delta t}$, determined from the length Δx and timescales Δt in lattice units. The expressions for $f_j^{(k),\text{eq}}$ and $S_j^{(k)}$ and the corresponding macroscopic variables are given in Table I.

The calculations are performed on a finite Cartesian grid that represents a channel confined by the walls in the y direction but extends infinitely in the x direction. The constraints of the geometry of the channel are imposed using the boundary conditions. In particular, the infinite length of the channel is implemented using the periodic boundary conditions in the x direction. In the y direction, however, the presence of the wall is incorporated using the midgrid bounceback scheme. Consequently, the no-flux boundary condition, neutral wetting behavior, and no-slip condition are imposed for reactive species (1 and 2), phase-field variable, and fluids, respectively [44].

D. Choice of parameters

The lattice Boltzmann simulations are performed on a domain of length 800 units with a droplet of 80 lattice units placed in it; the height of the channel, however, is varied according to $H = 80\alpha$. (Recall that α represents the ratio of the channel height to the droplet diameter.) The relaxation times for advection-diffusion equations τ_1 and τ_2 are chosen as 0.800 and 0.503, respectively; these values correspond to the diffusivities of c_1 and c_2 as 0.100 and 0.010. The density of the fluid is taken as unity and the relaxation times for the

TABLE I. Expressions for equilibrium distribution functions and the source terms used to determine the macroscopic variables. Here $\Gamma_j = \boldsymbol{w}_j[1 + \frac{\boldsymbol{e}_j\cdot\boldsymbol{u}}{c_s^2} + \frac{(\boldsymbol{e}_j\cdot\boldsymbol{u})^2}{2c_s^4} - \frac{\boldsymbol{u}\cdot\boldsymbol{u}}{2c_s^2}]$, $\chi = 1$, $\boldsymbol{w}_0 = \frac{4}{9}$, $\boldsymbol{w}_{1,2,3,4} = \frac{1}{9}$, and $\boldsymbol{w}_{5,6,7,8} = \frac{1}{36}$.

k	$f_j^{(k),\mathrm{eq}}$	$S_j^{(k)}$	Macroscopic variable
1, 2	$f_j^{(k),\mathrm{eq}} = \begin{cases} w_j[\frac{\chi\mu_k}{c_s^2} + c_k(\Gamma_j - w_j)], & j = 1\text{–}8 \\ c_k - \sum_{j=1}^{8} f_j^{(k),\mathrm{eq}}, & j = 0 \end{cases}$	$S_j^{(k)} = \begin{cases} J_k, & \phi \geqslant 0.5 \\ -(c_k - c_k^{\mathrm{bulk}}), & \phi < 0.5 \end{cases}$	$c_k = \sum_j f_j^{(k)}$
3	$f_j^{(k),\mathrm{eq}} = \phi\Gamma_j + \frac{w_j M}{c_s^2}[\frac{4}{\zeta}\phi(1-\phi)](\boldsymbol{e}_j\cdot\hat{\boldsymbol{n}})$	$S_j^{(k)} = 0$	$\phi = \sum_j f_j^{(k)}$
4	$f_j^{(k),\mathrm{eq}} = pw_j + \rho c_s^2(\Gamma_j - w_j)$	$S_j^{(k)} = \Delta t\Gamma_j(\boldsymbol{e}_j - \boldsymbol{u})\cdot\boldsymbol{F}_s$	$p = \sum_j f_j^{(k)}$
			$\boldsymbol{u} = \frac{1}{\rho c_s^2}\sum_j f_j^{(k)}\boldsymbol{e}_j + \frac{\Delta t}{2\rho}\boldsymbol{F}_S$

phase field parameter (τ_3) and fluid (τ_4) are chosen as 1.000 and 1.500, respectively; these values represent the interface mobility $M = \frac{1}{6}$ and kinematic viscosity of the fluid $\nu = \frac{1}{3}$. The parameters pertaining to the chemical potentials γ_1 and γ_2 are taken to be equal to 0.05. The BZ-reaction parameters inherent in the Oregonator model are chosen based on the standard recipe [38,45,46], which corresponds to the sustained chemical oscillations [40], as $a = 0.001$, $b = 0.550$, and $\epsilon = 0.0152$.

In order to map the simulation parameters to physical units we choose the lattice spacing $\Delta x = 0.0125$ mm and by comparing the droplet velocities, observed in simulations and experiments, we calculate the timescale $\Delta t = 0.1$ ms. We run simulations for up to 500 000 timesteps, which corresponds to an observation time window 50 s. The viscosity of squalene oil is chosen as a reference to map other quantities, given in Table II, into their corresponding physical units.

III. RESULTS AND DISCUSSION

In Fig. 2 we show the regimes of BZ oscillations and validate our LBM implementation by comparing it with the finite-difference methodology (FDM). In particular, Fig. 2(a) shows the bifurcation curve in ϵ vs b phase space, whereas in Figs. 2(b) and 2(c) we compare the time evolution of c_1 and c_2, corresponding to point P in Fig. 2(a), through the LBM and FDM; the trajectory of the system in the dynamical phase space of c_1 and c_2 is shown in Fig. 2(d).

The bifurcation curve in Fig. 2(a) is obtained from Eq. (6) using b as the bifurcation parameter. It is observed that as the value of b increases, ϵ initially increases, reaches a maximum, and then decreases, thereby encapsulating a region bounded by the abscissa and itself. Within this region, $\mathrm{Tr}(M_J) > 0$ and hence sustained chemical oscillations are observed in the BZ reaction. Mathematically speaking, as one travels from point P to higher values of ϵ (for a fixed b) the steady state of the system gains stability by Hopf bifurcation and therefore sustained time-periodic oscillations transform into decayed oscillations [see the insets in Fig. 2(a)]. Similar behavior is observed at other points within the curve; however, the fixed points, represented by c_1^{eq} and c_2^{eq}, of the system change with the change in b [see Eq. (4)].

Figures 2(b) and 2(c) show the time evolution of the concentrations of species 1 and 2, obtained using the FDM (solid line) and LBM (markers). We choose the initial condition as $c_1 = c_2 = 1$ and solve Eqs. (2) and (3) using the FDM and LBM, neglecting the diffusion and the convection effects. The concentration profiles of 1 and 2 periodically switch between low and high values, as the catalyst cycles between reduced and oxidized states; the latter state is indicated by $c_2 = c_2^{\max}$

TABLE II. Mapping between simulation and physical parameters.

Parameter	LB units	Physical units
lattice spacing Δx	1	0.0125 mm
unit time step Δt	1	0.1 ms
viscosity ν	1/3	10^{-2} Pa s
droplet diameter D	40	1 mm
surface tension σ	0.05	1 mN/m

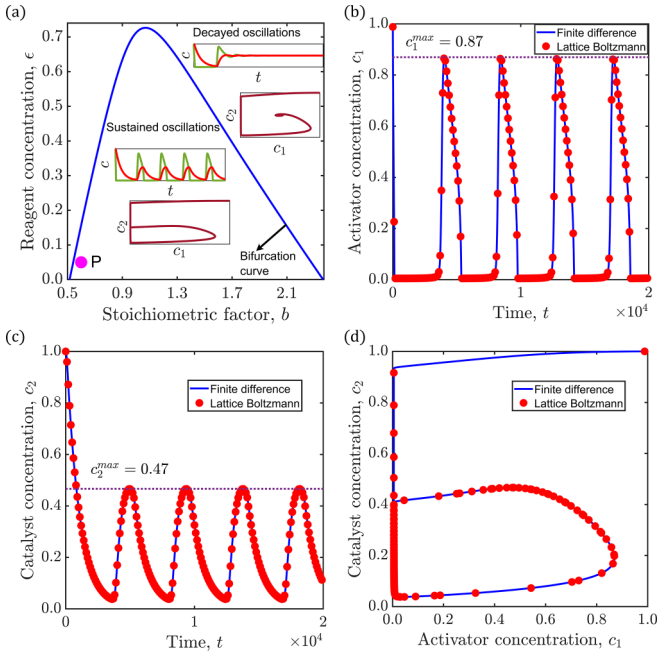

FIG. 2. Different regimes of BZ oscillation and its validation. (a) Bifurcation curve in ϵ vs b phase space that demarcates the sustained (below the curve) and decayed (above the curve) oscillations regimes. (b) and (c) Temporal evolution of the concentration of the reactive species 1 and 2, corresponding to point P in (a). Here $c_1^{\max}$ and $c_2^{\max}$ are the maximum thresholds of c_1 and c_2, respectively. (d) Chemical trajectory of the system in dynamical phase space (c_1, c_2).

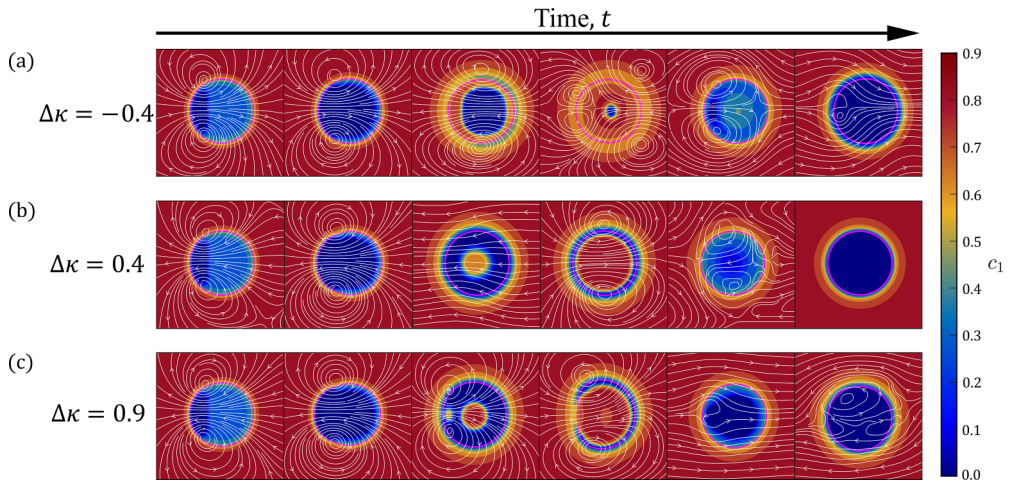

FIG. 3. Time evolution of the concentration and velocity field in the vicinity of the droplet for various $\Delta\kappa$. The solid white lines with arrows are streamlines. The background color represents the concentration of c_1 when the catalyst is in oxidized (red) and reduced (blue) states. The droplet-fluid interface is marked with in magenta.

in Fig. 2(c) and correspondingly $c_1 = c_1^{\max}$ in Fig. 2(b). It is observed from Fig. 2(c) that the variation in the values of c_2 is gradual, unlike the variation in c_1 shown in Fig. 2(b), where it mostly remains at low value and reaches its peak value for a very short period of time. These observations are consistent with the activator-inhibitor kinetics of the BZ reaction. The sustained periodic oscillations at point P represent the limit cycle shown in Fig. 2(d). In essence, Fig. 2 replicates the already known behavior of the BZ reaction and shows that our LBM results are in good agreement with the solutions obtained using the FDM.

A. Evolution of velocity field

In Fig. 3 we show the time evolution of the velocity field in the vicinity of the droplet, resulting from the BZ reaction inside the droplet, for different values of $\Delta\kappa$. The droplet is placed at the center of the channel of 800×240 ($\alpha = 3$) dimensions; however, in Fig. 3 an area of only 160×160 dimensions is shown with the frame of reference that moves with the droplet. Thus, in the timed snapshots shown in Fig. 3, the droplet seems to be stationary, whereas the velocity field, indicated by white lines with arrows (streamlines), evolves around it. The interface of the droplet is marked in magenta and the colors of contours correspond to the concentration of c_1, with blue and red representing the reduced and oxidized states, respectively. The initial concentrations of the reactive species are $c_1 = c_1^{\max}$ and $c_2 = c_2^{\max}$ across the entire computational domain that corresponds to point P in Fig. 2. The traveling (chemical) waves inside the droplet are triggered by introducing an initial perturbation $c_2 = 1.1c_2^{\max}$ at the leftmost end of the droplet; we refer to this region as the initial nucleation site. Let us now examine the flow patterns in our system with the movement of the traveling waves across the droplet.

Figure 3 shows that, during the initial stages, the chemical composition of the droplet essentially remains identical, irrespective of $\Delta\kappa$, but the velocity vectors reverse directions as $\Delta\kappa$ changes sign. At the late stages, however, both the chemical behavior and the flow fields evolve very differently for each case shown in Fig. 3.

We start the discussion from Fig. 3(a), which corresponds to $\Delta\kappa < 0$, at the beginning of the redox cycle (first image). Due to the initial perturbation, the reducing front begins to emerge from the initial nucleation site and gradually expands across the entire BZ droplet (second image). In the meantime, the oxidizing fronts get nucleated at the interface, encapsulate almost the entire droplet, and start to move towards the center (third image). As a result, the droplet core, which has been in the reduced state, keeps on shrinking (fourth image) and eventually disappears completely. Subsequently, the reducing front starts at the droplet interface (fifth image), fills the entire droplet (sixth image), and the cycle repeats. The key observation here is that even though the nucleation site is initialized near the left end of the droplet, in the subsequent cycles, the nucleation fronts emanate close to the interface and converge at the off-center position within the droplet (see movie 1 in the Supplemental Material [47]). Depending upon the position of the nucleation site, the fluid velocity also gets readjusted accordingly. As interface regions with low concentrations have high surface tension (since $\Delta\kappa < 0$), the Marangoni stresses thus generated drive the fluid from high- to low-concentration regions; the resulting source-dipole velocity field is similar to that of neutral squirmers [48–52]. Consequently, the convective current induced within the droplet opposes the diffusive flux and thereby maintains the inhomogeneous distribution of c_1 (nucleation sites) resulting in the continuous fluid flow. In other words, the c_1 produced within the BZ droplet is continuously carried to the interface and therefore the reaction front nucleates at the droplet-fluid interface in subsequent cycles and converge at an off-center position retaining asymmetric reaction patterns.

In Fig. 3(b) we capture the active droplet dynamics when $\Delta\kappa$ is increased to 0.4. Evidently, unlike Fig. 3(a), here the reaction front gets nucleated at the droplet center after the initial perturbation and ultimately the fluid flow stops. The overall behavior of the BZ droplet in Fig. 3(b) is in stark contrast with the observations in Fig. 3(a) and is attributed to the reversal

of the Marangoni flow. As $\Delta\kappa > 0$, the interface regions with low concentrations correspond to low surface tension and thus the induced convective current within the droplet supports the diffusive flux. As a consequence, the concentration distribution of c_1 within the droplet gets homogenized, which shifts the nucleation site towards its center eventually, leading to cessation of Marangoni stresses and fluid flow (see movie 2 in [47]).

Interestingly, we observe a very different behavior for $\Delta\kappa = 0.9$, as depicted in Fig. 3(c). Unlike previous cases, two nucleation sites emanate inside the droplet (third image), one close to the initial nucleation site and the other at the droplet center. Eventually, both the nucleation sites merge and expand, oxidizing the entire droplet (fourth image). Moreover, unlike Fig. 3(b), the droplet becomes intermittently oblate and the continuous fluid flow is maintained at all times (see movie 3 in [47]). The increase in $\Delta\kappa$ to a high value, as is the case here, facilitates stronger coupling between the concentration and surface tension. Thus, even a slight variation in c_1 significantly increases the surface tension gradient which in turn enhances the Marangoni stresses, thereby generating stronger convective currents. These stresses result in higher fluid velocities that deform the droplet, as a consequence (fourth image). In addition, the induced convective currents, within the deformed droplet, become very high compared to diffusive flux and thus the inhomogeneity in c_1 and fluid flow are always maintained. We note that the two nucleation sites are observed only during the initial stages, possibly due to asymmetry introduced by droplet deformation.

To summarize, the BZ-reaction pattern inside the droplet and corresponding velocity field are sensitive to the sign and magnitude of $\Delta\kappa$. At low positive values of $\Delta\kappa$, the synergistic effect between convective and diffusive currents homogenize the concentration inside the droplet and thereby generate symmetric traveling waves. As a consequence, the surface tension gradients cannot be established, which eventually stops the fluid flow. At other values of $\Delta\kappa$, the convective currents in conjunction with droplet deformation prevent homogenization and continuously drive the fluid flow. Having discussed the qualitative description of fluid flow and the effect of $\Delta\kappa$, we characterize the effect of confinement and Marangoni flow upon the instantaneous and long-time dynamics of the BZ droplet.

B. Swimming speed and droplet trajectories

In Fig. 4 we investigate the effect of negative coupling $\Delta\kappa < 0$ on the swimming speed and trajectory of the droplet for size ratio $\alpha = 3$. Recall that the surface tension between the fluid-droplet interface is reduced, when $\Delta\kappa < 0$, with the increase in c_1. In Fig. 4, therefore, as $\Delta\kappa$ moves towards more negative values, the surface tension keeps decreasing from the reference value κ_0. The initial temporal evolution of the swimming speed of the droplet for various $\Delta\kappa$ is presented in Figs. 4(a) and 4(b); the insets of Figs. 4(a) and 4(b) depict the long-time behavior, i.e., over the complete simulation. In particular, Fig. 4(a) shows the variation in swimming speed for less negative values of $\Delta\kappa$, while Fig. 4(b) shows the behavior for more negative values. On the other hand, the droplet trajectories and the distance d traveled by the droplet

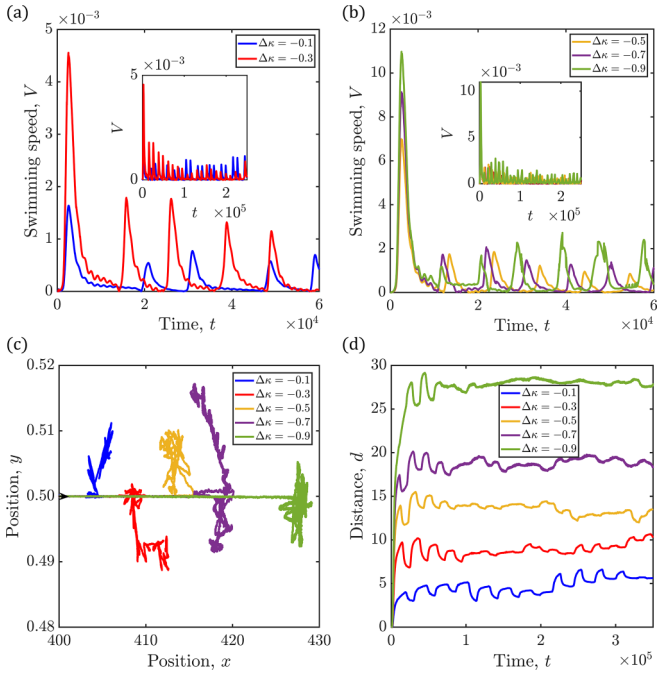

FIG. 4. Motion of the BZ droplet when $\Delta\kappa < 0$ and $\alpha = 3$. The temporal evolution of the swimming speed of the droplet is shown for (a) less negative and (b) more negative values of $\Delta\kappa$; the insets depict the long-time dynamics. (c) Trajectory of the active BZ droplet with the initial location and propulsion direction marked by an arrow. (d) Temporal evolution of the distance covered by the BZ droplet.

with respect to its initial location are given in Figs. 4(c) and 4(d), respectively. For comparison purposes, the ordinate of the droplet trajectory has been scaled with the channel height.

Figures 4(a) and 4(b) clearly show that the swimming speed exhibits time-periodic oscillations irrespective of the value of $\Delta\kappa$. In particular, the amplitude of oscillations in the droplet speed gradually decreases during the initial instants but is sustained with the passage of time; the amplitude, however, increases with the decrease in $\Delta\kappa$ from -0.1 to -0.3. A similar trend is also observed in Fig. 4(b), where even larger negative values of $\Delta\kappa$ have been used. In short, Figs. 4(a) and 4(b) demonstrate that the swimming speed of the droplet increases as $\Delta\kappa$ becomes more negative and the motion remains the same irrespective of its value. Likewise, the frequency of oscillations in the swimming speed also increases as $\Delta\kappa$ becomes more negative (see Sec. S1 of [47]). It is worth mentioning that the oscillations in swimming speed of the BZ droplet depicted here are consistent with experimental observations reported in the literature [9–11,41]. Our results, however, additionally demonstrate that the choice of a surfactant can be a key factor in achieving higher droplet velocities.

The oscillatory behavior of the swimming speed can be understood based on the reaction patterns shown in Fig. 3(a). When $\Delta\kappa < 0$, the reaction patterns are asymmetric about the droplet center due to the nucleation of the reaction wave front close to the interface. This asymmetry in the reaction patterns induces the gradient in surface tension that eventually drives the droplet motion. The time-periodic oscillations in swimming speed arise because the direction of traveling

waves within the droplet keeps on reversing as it switches between the reduced and oxidized states. On the other hand, as $\Delta\kappa$ becomes more negative, the surface tension gradients get amplified [see Eq. (14)] and thus even minute differences in c_1 at the droplet-fluid interface are capable of producing stronger flows; the swimming speed of the droplet therefore increases with the decrease in $\Delta\kappa$. Strong flows have an additional effect of enhancing the frequency of chemical oscillations in the BZ reaction [53]. Thus, as $\Delta\kappa$ becomes more negative, the frequency of oscillations in the swimming speed also increases (see Sec. S1 of [47]).

Let us now analyze the droplet trajectories in relation to the $\Delta\kappa$ using Fig. 4(c). In all the cases, we observe that the droplet, when placed symmetrically in the channel, moves along the centerline and exhibits linear motion (straight-line trajectory) and subsequently drifts towards one of the channel walls. The motion towards the wall, however, is non-monotonic, i.e., the direction of the droplet's motion keeps switching back and forth. It is evident from Fig. 4(c) that the initial straight-line distance traveled by the droplet, before the transition to the jittery motion, increases as $\Delta\kappa$ becomes more negative. This transition is also captured in Fig. 4(d), wherein the distance traveled by the droplet d initially increases with time and then continuously wavers around the mean position. Although the jittery motion of the droplet depicted in Figs. 4(c) and 4(d) is consistent with the experiments [2,11,48], our results demonstrate that high-speed straight-line motion can be achieved by tuning the properties of the surfactant. Recently, high-speed directional motion of the BZ droplets has been demonstrated experimentally [13] through the use of nanocatalysts.

Nonetheless, the migration of the droplet towards the wall requires the disruption of top-down symmetry about the channel centerline, which happens in the following manner. As shown in Fig. 3(a), in the initial instants the oxidizing front originates close to the droplet interface, travels inward, and converges on the channel centerline but is off-center with respect to the droplet. A slight perturbation of the convergence point from the channel centerline breaks the top-down symmetry and thereby drives the droplet towards the wall. Statistically, the droplet can move either towards the bottom or top wall but the outcome is highly sensitive to the initial conditions. As far as the periodic switch in the direction of motion of the droplet, while moving towards the wall, is concerned, it is due to the periodic reversal in the direction of the traveling chemical wave.

In Fig. 5 we perform an analysis similar to that in Fig. 4 but for $\Delta\kappa > 0$, i.e., Figs. 5(a)–5(d) have a one-to-one correspondence with Figs. 4(a)–4(d). Specifically, the temporal evolution of the swimming speed of the droplet for various $\Delta\kappa$ is shown in Figs. 5(a) and 5(b), while the trajectories of the droplets and the corresponding distances traveled by the droplet are shown in Figs. 5(c) and 5(d), respectively.

Unlike Fig. 4, in Fig. 5 ($\Delta\kappa > 0$) the droplet dynamics shows qualitatively different characteristics with the variation of $\Delta\kappa$. In particular, at lower values of $\Delta\kappa$ [Fig. 5(a)] the droplet speed exhibits periodic oscillations with decreasing amplitude that ultimately dies down at later times [see the inset in Fig. 5(a)]. At higher values of $\Delta\kappa$ [Fig. 5(b)], however, the droplet speed exhibits time-periodic oscillations. In

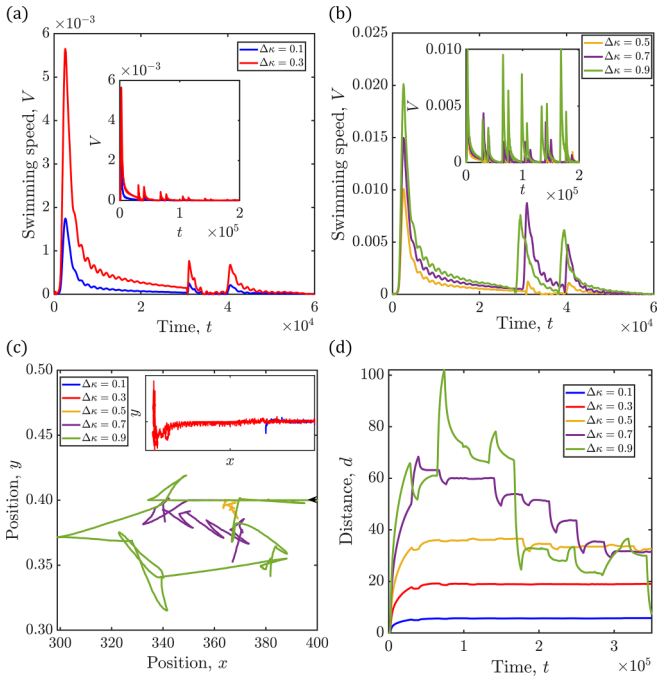

FIG. 5. Motion of the BZ droplet when $\Delta\kappa > 0$ and $\alpha = 3$. The temporal evolution of the swimming speed of the droplet is shown for (a) low and (b) high values of $\Delta\kappa$; the insets depict the long-time dynamics. (c) Trajectory of the active BZ droplet with the initial location and propulsion direction marked by an arrow. (d) Temporal evolution of the distance covered by the BZ droplet.

short, the comparison between Figs. 4(a) and 4(b) with the respective Figs. 5(a) and 5(b) reveals the existence of two regimes of droplet motion for positive $\Delta\kappa$, namely, stationary and sustained motion. We note that, irrespective of the value of $\Delta\kappa$, the first oscillation is characterized by a single peak whereas two short-interval peaks appear at subsequent times.

The observations in Figs. 5(a) and 5(b) are consistent with the reaction-diffusion patterns and can be exemplified by the corresponding velocity fields depicted in Fig. 3. Recall that for $\Delta\kappa > 0$ the convective and diffusive fluxes are in the same direction, which tends to homogenize the concentrations of reactants inside the circular droplet, which leads to radial chemical waves incapable of generating any Marangoni stresses for small values of $\Delta\kappa$. The homogenization-induced cessation of Marangoni flow and swimming speed has been reported in experiments [9] in diffusion-dominant scenarios. Similar to Fig. 4(a), however, the swimming speed of the droplet and the fluid velocity increase with an increase in $\Delta\kappa$ due to an increase in the strength of coupling between the surface tension and concentration c_1. This strong fluid velocity deforms the droplet into a noncircular asymmetric shape [see Fig. 3(c)] that prevents the emergence of symmetric reaction-diffusion patterns in the droplet. Thus, the homogenization effect, caused by the convective and diffusive fluxes, gets counterbalanced, which in turn preserves the surface tension gradients and maintains the Marangoni flow. For large values of $\Delta\kappa$ [Fig. 5(b)], therefore, the droplet exhibits sustained oscillations in the swimming speed due to the continuous generation of asymmetric reaction patterns, similar to Fig. 4(b).

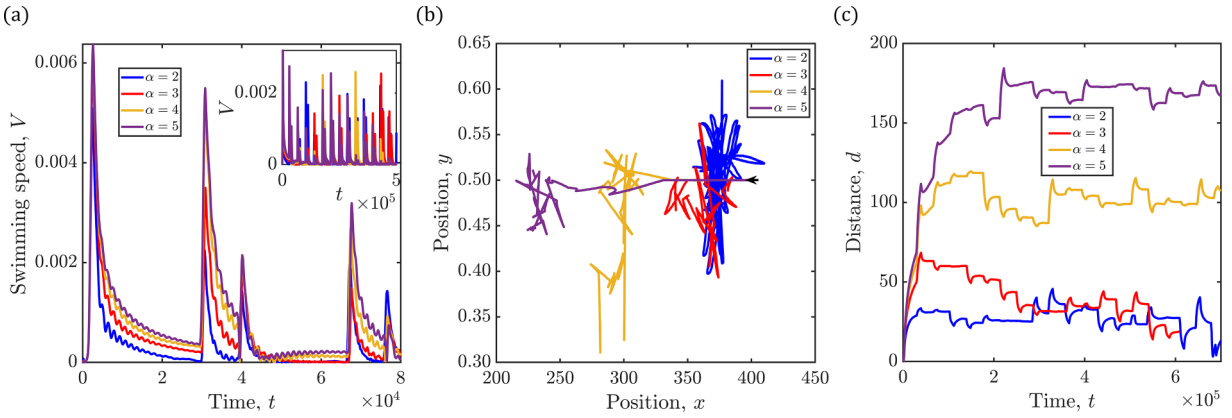

FIG. 6. Effect of size ratio α on the (a) swimming speed, (b) trajectory, and (c) distance covered by the BZ droplet for $\Delta\kappa = 0.7$. The inset in (a) depicts the long-time behavior.

In contrast, at low values of $\Delta\kappa$ [Fig. 5(a)] the asymmetry in the droplet shape is not enough to prevent the homogenization of reactants inside the droplet and the droplet stops moving eventually. Moreover, unlike Fig. 4, the frequency of oscillations is independent $\Delta\kappa$ (see Sec. S2 of [47]) and the appearance of two short-interval peaks is attributed to the inherent chemical oscillations of the BZ reaction [see Fig. S2(a) of [47]]. Specifically, the first peak appears when the BZ reaction inside the droplet switches from the reduced to the oxidized state, while the second peak appears when it switches back to the reduced state [see Fig. S2(a) of [47]]. Thus, for $\Delta\kappa > 0$, the diffusive and convective effects only affect the amplitude of the swimming speed but not its frequency.

As a consequence of two different behaviors in swimming speeds, obtained by varying $\Delta\kappa$, we observe two types of droplet motion, depicted as trajectories in Fig. 5(c). When $\Delta\kappa < 0.5$, the droplet translates a very minimal distance along the channel centerline and becomes stationary [inset of Fig. 5(c)]. Conversely, for $\Delta\kappa \geqslant 0.5$, the droplet breaks the top-down symmetry and moves away from the channel centerline, exhibiting a sustained linear motion with intermittent rotations that resembles run-and-tumble trajectories. This behavior can also be inferred from Fig. 5(d), wherein for low values of $\Delta\kappa$ ($\Delta\kappa < 0.5$), the distance increases initially but attains a constant value at later times, indicating cessation of the droplet's motion. For a higher value of $\Delta\kappa$, however, the distance continuously varies with time, signifying sustained motion of the droplet. In addition, the comparison between Figs. 5(d) and 4(d) reveals that the droplets cover significantly larger distances when $\Delta\kappa$ values are large and positive.

The results shown in Fig. 5 qualitatively resonate with the reaction-diffusion patterns and velocity field depicted in Fig. 3 and can be understood as follows. The initial motion of the droplet along the channel centerline, irrespective of $\Delta\kappa$, is attributed to the off-center location of the nucleation spot (set by the initial condition). When $\Delta\kappa$ is small, the nucleation spot quickly moves towards the center of the droplet [see Fig. 3(b)], thereby generating symmetrical reaction-diffusion patterns inside the droplet. The overall effect of these processes is that the droplet translates only for a short duration and then becomes stationary. On the other hand, when $\Delta\kappa$ is large, the symmetrical reaction-diffusion patterns emanating inside the droplet are hindered because of the droplet deformation. Thus, the symmetry is broken and the droplet starts to move towards either of the walls. In the meantime, the reaction front reverses its direction and makes the droplet move in the opposite direction. The combination of these two processes results in a looping trajectory for the droplet but with a dominant linear motion, as is evident in Fig. 5(c).

Based on the foregoing discussion related to Figs. 4 and 5, an active droplet exhibits two kinds of motion, namely, stationary and sustained, depending on the sign and magnitude of $\Delta\kappa$. Specifically, the droplet becomes stationary after a short initial motion for low and positive $\Delta\kappa$, but shows sustained long-time motion otherwise.

C. Effect of confinement on droplet dynamics

Figure 6 shows the effect of confinement, quantified in terms of size ratio α, on the droplet's swimming speed [Fig. 6(a)], trajectory [Fig. 6(b)], and distance traveled by the droplet [Fig. 6(c)] at $\Delta\kappa = 0.7$. Figure 6(a) shows clearly that the droplet speed exhibits time-periodic oscillations that are sustained over the entire duration; the long-time behavior is shown in the inset. Qualitatively, the swimming speed of the droplet is independent of α; its value, however, increases as α increases, i.e., as the confinement gets weaker. The increase in the swimming speed with α can be analyzed by the interplay between the Marangoni stresses and the resistance offered by channel walls. To elaborate, for a given driving force (Marangoni stresses) the increase in α decreases the resistance to fluid flow and thus results in large fluid velocities. As a consequence, stronger convective currents, which dominate over diffusion, are able to maintain large surface tension gradients that further deform the droplet and assist the fluid motion via asymmetric reaction patterns. Conversely, as the confinement becomes stronger (decrease in α) and consequently the flow becomes weaker, the deformation of the droplet is suppressed. The distribution of surface active species therefore becomes less asymmetric, which, as a result, produces weaker Marangoni stresses, which in turn leads to lower droplet velocities.

Let us now analyze the droplet trajectories in relation to α using Fig. 6(b). In all cases, we observe that droplet initially moves along the channel centerline and eventually deviates from the centerline and exhibits a sustained motion. The

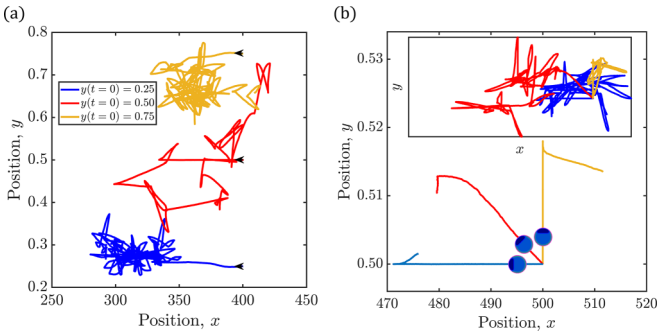

FIG. 7. Effect of (a) initial location of the droplet within the channel and (b) initial position of the nucleation site within the droplet on the trajectory of the active BZ droplet for $\alpha = 3$ and $\Delta\kappa = 0.7$. The inset in (b) represents the long-time behavior.

persistence of linear motion along the channel centerline increases with the increase in α and is attributed to the following reasons. The initial linear motion along the centerline is due to the top-down symmetry of the off-center nucleation site set during the beginning of the simulations. As confinement gets weaker (increase in α) strong flows assist the linear motion of the droplet along the channel centerline. However, once the initial top-down symmetry is broken, irrespective of α, droplets exhibit a looping trajectory that resembles the run-and-tumble behavior identified in Fig. 5. Recall that the run-and-tumble trajectory corresponds to the periodic reversal in the direction of the propagation of the chemical waves within the droplet. The time evolution of the distance traveled by the droplet (d), shown in Fig. 6(c), also corroborates this run-and-tumble behavior. In particular, Fig. 6(c) shows an initial monotonic increase in d with time that represents the linear droplet motion along the channel centerline. At later times this linear motion transitions to back-and-forth motion, which depicts the run-and-tumble characteristics. Furthermore, in agreement with Fig. 6(b), we observe from Fig. 6(c) that d increases as α increases. Evidently, the comparison of Fig. 6 with Fig. 5 reveals that α and $\Delta\kappa$ have a similar impact on the droplet dynamics.

D. Sensitivity of the BZ droplet dynamics to initial conditions

In Fig. 7 we explore the effect of the initial location of the droplet [in Fig. 7(a)] in the channel and the initial nucleation site [in Fig. 7(b)] on the droplet dynamics at $\Delta\kappa = 0.7$ and $\alpha = 3.0$; the droplet behavior is quantified by the trajectory of its motion inside the channel. In Fig. 7(a) the three trajectories are shown wherein the droplet is placed at the center (red) and near the top (yellow) and bottom (blue) walls of the channel; these respective initial locations correspond to $y = 0.50, 0.75$, and 0.25 in Fig. 7(a). We can clearly observe from Fig. 7(a) that irrespective of the initial location, the droplet exhibits linear motion during the initial instants but the persistence of the linear motion is quite sensitive to the location of the droplet. For instance, the droplet endures straight-line motion for a long-time when the droplet is initially placed close to the centerline (red curve), whereas it quickly deviates from the straight-line trajectory when it is placed close to the walls (yellow and blue curves). Likewise, the long-time behavior is also affected by the initial location of the droplet. The trajectories in Fig. 7(a) show that when the droplet is initially placed along the channel centerline its motion is predominantly linear. On the other hand, the droplet initially placed close to one of the channel walls traces a path dominated by zigzag motion. The motion exhibited by the droplet can be analyzed based on the top-down symmetry of the droplet with respect to the channel. The channel centerline is a position with top-down symmetry and therefore the droplet translates along the channel centerline until this symmetry is broken via reaction-diffusion phenomena [as explained in Figs. 3(c) and 5]. In contrast, the top-down symmetry is naturally broken when the droplet is placed at the off-center locations within the channel and thus the zigzag motion of the droplet kicks in after a relatively short straight-line motion. Moreover, the zigzag motion of the droplet is facilitated by its proximity to the channel wall as this droplet experiences a stronger resistance, compared to the droplet located at the channel centerline, and as a consequence the net distance traveled by the droplet placed off-center is significantly small. In short, the symmetry associated with the droplet's initial location in conjunction with the resistance from the walls ultimately governs the droplet trajectory and the distance it travels.

Up to now we have explored the droplet motion with the initial nucleation center restricted only to the leftmost end of the droplet. In general, however, this is not the case and the nucleation point can be located randomly anywhere inside the droplet. Recent experiments on nanocatalyzed BZ droplets [13] indicate that the initial direction of the droplet's motion might be attributed to the location of the nucleation site within the droplet. In Fig. 7(b), therefore, we explore this aspect by tracing the droplet trajectories with different locations of the nucleation site. In particular, we set the initial nucleation centers, in Fig. 7(b), at the leftmost, left-diagonal, and top ends of the droplet; $\Delta\kappa$ and α are set to 0.7 and 3.0, respectively. The trajectories in Fig. 7(b) clearly reveal that the initial motion of the droplet initially is in the direction of the nucleation site, which evidently is opposite to the propagation of the chemical waves [Figs. 3(b) and 3(c)]. Just like the previous scenarios [Figs. 5–7(a)], the long-time behavior of the droplet's motion remains rotation dominant irrespective of the initial location of the nucleation site. Intuitively, the initial linear motion of the droplet, opposite to the direction of chemical wave, is due to the initial Marangoni flow established by the regions of low surface tension (initial nucleation site) and high surface tension (opposite side of the initial nucleation site). After the first few reaction cycles, irrespective of the initial nucleation site, traveling waves emanate from within the droplet as depicted in Fig. 3(c), resulting in a rotation-dominant trajectory with smaller displacements [inset of Fig. 7(b)]. Based on the same lines of argument, the droplet's initial motion is envisaged to be in the direction of the traveling chemical waves [see Fig. 3(a) and 4(c)] when $\Delta\kappa < 0$.

IV. CONCLUSION

We have investigated the propulsion dynamics of an active droplet driven by a self-oscillating BZ reaction in a two-dimensional channel using the LBM. Specifically, we have

modeled the BZ kinetics using the two-variable Oregonator model and considered the activator as surface active. We primarily focused on understanding the role of the strength and nature of coupling between the surface tension and the concentration of activator ($\Delta\kappa$) on the instantaneous and long-time dynamics of the BZ droplet. We also analyzed the effect of confinement (α) and initial conditions on the droplet dynamics. In essence, our investigations revealed the sensitivity of the different possible behaviors of an active BZ droplet, namely, stationary and sustained motion, to $\Delta\kappa$ and the size ratio (α).

The comparison between positive and negative values of $\Delta\kappa$ revealed the mechanism underlying the motion of the BZ droplet in terms of convective and diffusive fluxes. If the diffusive and convective fluxes are in the opposite direction, i.e., for $\Delta\kappa < 0$, a sustained fluid flow and droplet motion is observed. On the other hand, the coordination between both the fluxes observed for $\Delta\kappa > 0$ results in the homogenization of the reactive species, eventually leading to the cessation of flow and droplet motion. We identified that the deformation of the droplet can prevent the generation of symmetric patterns and results in the transition from stationary to sustained droplet motion with an increase in $\Delta\kappa$. In addition, from the comparison of the sustained motion, for both $\Delta\kappa < 0$ and $\Delta\kappa > 0$, we demonstrated that the trajectories with dominant linear motion accompanied by significant displacements occur for large and positive $\Delta\kappa$.

Our investigation further revealed that dominant linear motion can be prolonged, with higher swimming speeds, when the confinement is weaker (large α) and eventually makes the droplet traverse large distances. Finally, in accord with the experiments, tuning the initial conditions has enabled us to control the motion of the droplet. Specifically, by varying the location of the initial nucleation, the starting direction of the droplet's motion can be controlled; however, the long-time behavior is independent of the initial conditions. We envisage that better control over the trajectory of the droplet can be achieved by controlling the location of the nucleation site in the subsequent reaction cycles as well through the use of external stimuli such as light and background flow of the surrounding fluid. Our findings can be utilized to develop synthetic chemomechanically driven cell models and targeted delivery microfluidic platforms.

ACKNOWLEDGMENTS

The authors thank Chaitra Borkar for preliminary investigations and acknowledge funding support from IIT Gandhinagar.

[1] C. C. Maass, C. Krüger, K. Krüger, S. Herminghaus, and C. Bahr, Swimming droplets, Annu. Rev. Condens. Matter Phys. **7**, 171 (2016).

[2] S. Michelin, Self-propulsion of chemically active droplets, Annu. Rev. Fluid Mech. **55**, 77 (2023).

[3] L. N. Carenza, G. Gonnella, and G. Negro, Motility and self propulsion of active droplets, arXiv:2208.11386.

[4] L. Giomi and A. Desimone, Spontaneous Division and Motility in Active Nematic Droplets, Phys. Rev. Lett. **112**, 147802 (2014).

[5] L. N. Carenza, G. Gonnella, D. Marenduzzo, and G. Negro, Rotation and propulsion in 3D active chiral droplets, Proc. Natl. Acad. Sci. USA **116**, 22065 (2019).

[6] Z. Huang, T. Omori, and T. Ishikawa, Active droplet driven by a collective motion of enclosed microswimmers, Phys. Rev. E **102**, 022603 (2020).

[7] M. Rajabi, H. Baza, T. Turiv, and O. D. Lavrentovich, Directional self-locomotion of active droplets enabled by nematic environment, Nat. Phys. **17**, 260 (2020).

[8] L. J. Ruske and J. M. Yeomans, Morphology of Active Deformable 3D Droplets, Phys. Rev. X **11**, 021001 (2021).

[9] N. J. Suematsu, Y. Mori, T. Amemiya, and S. Nakata, Oscillation of speed of a self-propelled Belousov-Zhabotinsky droplet, J. Phys. Chem. Lett. **7**, 3424 (2016).

[10] N. J. Suematsu, K. Saikusa, T. Nagata, and S. Izumi, Interfacial dynamics in the spontaneous motion of an aqueous droplet, Langmuir **35**, 11601 (2019).

[11] N. J. Suematsu, Y. Mori, T. Amemiya, and S. Nakata, Spontaneous mode switching of self-propelled droplet motion induced by a clock reaction in the Belousov-Zhabotinsky medium, J. Phys. Chem. Lett. **12**, 7526 (2021).

[12] S. J. S. Jamaluddin, K. Khaothong, M. R. Tinsley, and K. Showalter, Photochemical motion control of surface active Belousov-Zhabotinsky droplets, Chaos **30**, 083143 (2020).

[13] D. J. P. Kumar, C. Borkar, and P. Dayal, Fast-Moving self-propelled droplets of a nanocatalyzed Belousov-Zhabotinsky reaction, Langmuir **37**, 12586 (2021).

[14] V. S. Akella, D. K. Singh, S. Mandre, and M. M. Bandi, Dynamics of a camphoric acid boat at the air-water interface, Phys. Lett. A **382**, 1176 (2018).

[15] H. Kitahata, N. Yoshinaga, K. H. Nagai, and Y. Sumino, Spontaneous motion of a droplet coupled with a chemical wave, Phys. Rev. E **84**, 015101 (2011).

[16] K. Shioiri, T. Sakurai, and H. Kitahata, Control of the self-motion of a ruthenium-catalyzed Belousov-Zhabotinsky droplet, J. Phys. Chem. C **116**, 26805 (2012).

[17] N. J. Suematsu, Y. Miyahara, Y. Matsuda, and S. Nakata, Self-Motion of a benzoquinone disk coupled with a redox reaction, J. Phys. Chem. C **114**, 13340 (2010).

[18] S. Nakata, Y. Matsuda, Y. S. Ikura, A. Takeda, and S. Izumi, Mode change in the self-motion of a benzoquinone disk coupled with a NADPH system, Chemphyschem **13**, 520 (2012).

[19] Y. Xiao, S. Zarghami, K. Wagner, P. Wagner, K. C. Gordon, L. Florea, D. Diamond, and D. L. Officer, Moving droplets in 3D using light, Adv. Mater. **30**, 35 (2018).

[20] P. Dayal, O. Kuksenok, and A. C. Balazs, Reconfigurable assemblies of active, autochemotactic gels, Proc. Natl. Acad. Sci. USA **110**, 431 (2013).

[21] S. di Talia and M. Vergassola, Waves in embryonic development, Annu. Rev. Biophys. **51**, 327 (2022).

[22] J. J. Tyson, From the Belousov-Zhabotinsky reaction to biochemical clocks, traveling waves and cell cycle regulation, Biochem. J. **479**, 185 (2022).

[23] H. Kitahata, R. Aihara, N. Magome, and K. Yoshikawa, Convective and periodic motion driven by a chemical wave, J. Chem. Phys. **116**, 5666 (2002).

[24] T. Toyota, N. Maru, M. M. Hanczyc, T. Ikegami, and T. Sugawara, Self-propelled oil droplets consuming "fuel" surfactant, J. Am. Chem. Soc. **131**, 5012 (2009).

[25] Y. Sumino, N. Magome, T. Hamada, and K. Yoshikawa, Self-Running Droplet: Emergence of Regular Motion from Nonequilibrium Noise, Phys. Rev. Lett. **94**, 068301 (2005).

[26] S. Herminghaus, C. C. Maass, C. Krüger, S. Thutupalli, L. Goehring, and C. Bahr, Interfacial mechanisms in active emulsions, Soft Matter **10**, 7008 (2014).

[27] D. J. P. Kumar, K. R. Reddy, and P. Dayal, 0D-2D heterostructures as nanocatalysts for self-oscillating reactions: An investigation into chemical kinetics, Phys. Chem. Chem. Phys. **22**, 24516 (2020).

[28] K. Torbensen, F. Rossi, S. Ristori, and A. Abou-Hassan, Chemical communication and dynamics of droplet emulsions in networks of Belousov-Zhabotinsky micro-oscillators produced by microfluidics, Lab Chip **17**, 1179 (2017).

[29] S. Yabunaka, T. Ohta, and N. Yoshinaga, Self-propelled motion of a fluid droplet under chemical reaction, J. Chem. Phys. **136**, 074904 (2012).

[30] N. Yoshinaga, Spontaneous motion and deformation of a self-propelled droplet, Phys. Rev. E **89**, 012913 (2014).

[31] M. Schmitt and H. Stark, Marangoni flow at droplet interfaces: Three-dimensional solution and applications, Phys. Fluids **28**, 012106 (2016).

[32] M. Morozov and S. Michelin, Self-Propulsion near the onset of Marangoni instability of deformable active droplets, J. Fluid Mech. **860**, 711 (2019).

[33] F. Fadda, G. Gonnella, A. Lamura, A. Tiribocchi, S. Guido, A. Scagliarini, and F. Toschi, Lattice Boltzmann study of chemically-driven self-propelled, Eur. Phys. J. E **40**, 112 (2017).

[34] K. Lippera, M. Morozov, M. Benzaquen, and S. Michelin, Collisions and rebounds of chemically active droplets, J. Fluid Mech. **886**, A17 (2020).

[35] S. Yabunaka and N. Yoshinaga, Collision between chemically driven self-propelled drops, J. Fluid Mech. **806**, 205 (2016).

[36] M. Schmitt and H. Stark, Swimming active droplet: A theoretical analysis, Europhys. Lett. **101**, 44008 (2013).

[37] K. Furtado, C. M. Pooley, and J. M. Yeomans, Lattice Boltzmann study of convective drop motion driven by nonlinear chemical kinetics, Phys. Rev. E **78**, 046308 (2008).

[38] J. J. Tyson and P. C. Fife, Target patterns in a realistic model of the Belousov-Zhabotinskii reaction, J. Chem. Phys. C **73**, 2224 (1980).

[39] M. M. M. Mazzotti and G. Serravalle, Belousov-Zhabotinskii oscillations reactor in a batch reactor, Chem. Eng. Sci. **49**, 681 (1993).

[40] V. Rajput and P. Dayal, Dynamical attributes of nanocatalyzed self-oscillating reactions via bifurcation analyses, J. Chem. Phys. **155**, 064902 (2021).

[41] S. Thutupalli and S. Herminghaus, Tuning active emulsion dynamics via surfactants and topology, Eur. Phys. J. E **36**, 91 (2013).

[42] P. H. Chiu and Y. T. Lin, A conservative phase field method for solving incompressible two-phase flows, J. Comput. Phys. **230**, 185 (2011).

[43] A. Fakhari and D. Bolster, Diffuse interface modeling of three-phase contact line dynamics on curved boundaries: A lattice Boltzmann model for large density and viscosity ratios, J. Comput. Phys. **334**, 620 (2017).

[44] T. Krüger, H. Kusumaatmaja, A. Kuzmin, O. Shardt, G. Silva, and E. M. Viggen, *The Lattice Boltzmann Method* (Springer International, Cham, 2017).

[45] S. K. Scott, *Chemical Chaos* (Clarendon, Oxford, 1993).

[46] S. K. Scott, *Oscillations, Waves, and Chaos in Chemical Kinetics* (Oxford University Press, Oxford, 1994).

[47] See Supplemental Material at http://link.aps.org/supplemental/10.1103/PhysRevE.106.065103 for figures depicting the correlation between the frequency of oscillations in swimming speed and BZ reaction kinetics.

[48] S. Thutupalli, R. Seemann, and S. Herminghaus, Swarming behavior of simple model squirmers, New J. Phys. **13**, 073021 (2011).

[49] P. Dwivedi, D. Pillai, and R. Mangal, Self-Propelled swimming droplets, Curr. Opin. Colloid Interface Sci. **61**, 101614 (2022).

[50] C. de Blois, M. Reyssat, S. Michelin, and O. Dauchot, Flow field around a confined active droplet, Phys. Rev. Fluids **4**, 054001 (2019).

[51] P. Dwivedi, A. Shrivastava, N. Tiwari, D. Pillai, and R. Mangal, Deforming active droplets in viscoelastic media, arXiv:2209.14348.

[52] J. S. Lintuvuori, A. T. Brown, K. Stratford, and D. Marenduzzo, Hydrodynamic oscillations and variable swimming speed in squirmers close to repulsive walls, Soft Matter **12**, 7959 (2016).

[53] Y. Y. Kalishyn, M. Rachwalska, and P. E. Strizhak, Stirring effect on the Belousov-Zhabotinsky oscillating chemical reactions in a batch. Experimental and modelling, Z. Naturforsch. A **65**, 132 (2010).